

A silanol-functionalized polyoxometalate with excellent electron transfer mediating behavior to ZnO and TiO₂ cathode interlayers for highly efficient and extremely stable polymer solar cells†

Marinos Tountas,^{ab} Yasemin Topal,^c Apostolis Verykios,^{ad} Anastasia Soultati,^a Andreas Kaltzoglou,^{id}^a Theodoros A. Papadopoulos,^{id}^e Florian Auras,^{id}^f Kostas Seintis,^d Mihalis Fakis,^{id}^d Leonidas C. Palilis,^d Dimitris Tsikritzis,^{id}^g Stella Kennou,^g Azhar Fakharuddin,^h Lukas Schmidt-Mende,^h Spyros Gardelis,^{id}ⁱ Mahmut Kus,^j Polycarpus Falaras,^{id}^a Dimitris Davazoglou,^a Panagiotis Argitis,^{id}^a and Maria Vasilopoulou ^{id}^{*a}

Combining high efficiency and long lifetime under ambient conditions still poses a major challenge towards commercialization of polymer solar cells. Here we report a facile strategy that can simultaneously enhance the efficiency and temporal stability of inverted photovoltaic architectures. Inclusion of a silanol-functionalized organic–inorganic hybrid polyoxometalate derived from a PW₉O₃₄ lacunary phosphotungstate anion, namely (nBu₄N)₃[PW₉O₃₄(tBuSiOH)₃], significantly increases the effectiveness of the electron collecting interface, which consists of a metal oxide such as titanium dioxide or zinc oxide, and leads to a high efficiency of 6.51% for single-junction structures based on poly(3-hexylthiophene):indene-C60 bisadduct (P3HT:IC₆₀BA) blends. The above favourable outcome stems from a large decrease in the work function, an effective surface passivation and a decrease in the surface energy of metal oxides which synergistically result in the outstanding electron transfer mediating capability of the functionalized polyoxometalate. In addition, the insertion of a silanol-functionalized polyoxometalate layer significantly enhances the ambient stability of unencapsulated devices which retain nearly 90% of their original efficiencies (T₉₀) after 1000 hours.

Introduction

The development of highly efficient, environmentally friendly alternative technologies for solar-energy conversion at low cost is essential due to the unprecedented growth in energy usage in recent years. Polymer solar cells (PSCs) have attracted growing attention over the past few decades because of their advantages in fabricating low cost, lightweight, flexible and large size light harvesting devices.^{1–3} For an optimized use of solar energy, however, efficient as well as stable PSCs are required. Since the first report on organic bulk heterojunction (BHJ) solar cells, substantial progress has been made towards device efficiencies above 10%.^{4,5} Aside from improvements in the design and synthesis of active materials,^{6–8} interface engineering, which usually comprises the insertion of appropriate transport interlayers, has emerged as a key factor for boosting the efficiency and stability of PSCs.^{9–13} Metal oxide-based semiconductors, in particular, zinc oxide (ZnO) and titanium dioxide (TiO₂), have been recognized as efficient cathode interlayers (CILs) in PSCs due to their excellent optical transparency, low-toxicity and

^a Institute of Nanoscience and Nanotechnology, National Centre for Scientific Research "Demokritos", 15310, Agia Paraskevi, Attiki, Greece.

E-mail: m.vasilopoulou@inn.demokritos.gr

^b School of Applied Mathematical and Physical Sciences, National Technical University of Athens, Zografou Campus, 15780 Athens, Greece

^c Pamukkale University Cal Vocational High School, 20700, Cal/Denizli, Turkey

^d Department of Physics, University of Patras, 26504 Patras, Greece

^e Department of Natural Sciences, University of Chester, Thornton Science Park, CH2 4NU, Chester, UK

^f Cavendish Laboratory, University of Cambridge, Cambridge CB3 0HE, UK

^g Department of Chemical Engineering, University of Patras, 26504 Patras, Greece

^h Department of Physics, University of Konstanz, 78457 Konstanz, Germany

ⁱ Solid State Physics Section, Physics Department, National and Kapodistrian University of Athens, Panepistimioupolis, 15784 Zografos, Athens, Greece

^j Chemical Engineering Department, Selcuk University, 42075 Konya, Turkey

solution-based fabrication.^{14–16} However, there are limitations in using as-deposited ZnO and TiO₂ firstly due to their moderate n-type conductivity, especially in the case of TiO₂, and secondly due to high recombination rates of photogenerated electron–hole pairs at surface trap states of metal oxides. Both effects hamper the efficiency of electron transfer towards the cathode contact.^{17–20} In addition, the relatively high work function (W_F) of ZnO and TiO₂ may lead to a significant electron extraction barrier at the metal oxide/organic interface. Furthermore, the incompatibility between hydrophilic metal oxides and hydrophobic polymers usually causes non-optimal surface coverage and macroscopic phase separation. All these result in inferior device performance and poor overall stability.

To overcome these limitations several strategies have been developed such as the implementation of appropriate surface modifiers, usually polyelectrolytes with acidic and amino groups,^{21–23} self-assembled monolayers (SAMs)^{24–26} and organic nano-dots,^{27–29} which optimize the W_F of the interlayers as well as the contact between the interlayers and the photoactive blend. However, these organic modifiers suffer from insulating properties, thus limiting the device efficiency. In contrast, doping of metal oxides with several elements^{30–34} and appropriate gas treatment^{35,36} have simultaneously increased their conductivity and passivated surface defects thus accelerating electron transfer towards the cathode extending their effectiveness as CILs in PSCs. Polyoxometalates (POMs), which represent a large family of environmentally friendly inorganic clusters, are promising candidates for multi-electron transfer catalysts, as they are stable against oxidative degradation and can receive a large number of electrons without deforming their structures.^{37,38} They were recently used by our group and others as cathode interlayers in PSCs with either the conventional or the inverted architecture due to their unique properties, such as facile processing from water or alcohol solutions, adequate electron mobility, and high transparency in the visible range.^{39–44} However, their possible aggregation when forming solid films from aqueous solutions may be extremely harmful to device performance and stability; consequently, it is rather unlikely for pristine POMs to be suitable for large-area production of PSCs. As yet, work to exploit appropriate concepts to simultaneously achieve superior electron transfer properties of POMs while also avoiding aggregation for successful application in PSCs is limited.^{43,44}

In order to utilize the unique advantages of POMs, we synthesized a *tert*-butyl silanol (*t*BuSiOH) functionalized POM-based complex containing the PW₉O₃₄ cluster with the lacunary Keggin structure namely (*n*Bu₄N)₃[PW₉O₃₄(*t*BuSiOH)₃] (chemical formula C₆₁H_{139.5}N_{3.5}PO₃₇Si₃W₉) (referred to as *t*BuSiOH-POM), which is inserted into the vicinity of the metal oxide/organic interface to allow superior electron transfer to TiO₂ and ZnO CILs. The effective anchoring of *t*BuSiOH-POM onto metal oxide substrates through silanol linkers results in the formation of a uniform POM film. The insertion of such a film into the device structure simultaneously offers a large decrease in the work function and an effective surface passivation of metal oxides increasing the device open-circuit voltage (V_{oc}). The presence of hydrophobic tertiary butyl groups^{45,46} decreases the surface energy of the

substrate resulting in the formation of homogeneous and closely packed photoactive films improving the device fill factor (FF). The outstanding electron transfer mediating capability of *t*BuSiOH-POM to metal oxides induces a large enhancement in the short-circuit current (J_{sc}). Consequently, when a *t*BuSiOH-POM layer is applied as the electron transfer mediator between the photoactive film, composed of a poly(3-hexylthiophene):indene-C60 bisadduct (P3HT:IC₆₀BA) blend, and the metal oxide, power conversion efficiencies (PCEs) of up to 6.51% were obtained. Besides we observed a remarkable temporal stability of intentionally unencapsulated cells which retain about 90% of their initial PCE (T_{90}) after 1000 h. Improved device performance was also obtained when using P3HT:[6,6]-phenyl-C71butyric acid methyl ester (PC₇₁BM) and poly[4,8-bis[(2-ethylhexyl)oxy]benzo[1,2-*b*:4,5-*b'*]dithiophene-2,6-diyl][3-fluoro-2-[(2-ethylhexyl)carbonyl]thieno[3,4-*b*]thiophenediyl](PTB7):PC₇₁BM as the photoactive blends while indium tin oxide (ITO) modified with *t*BuSiOH-POM worked effectively as an electron selective contact demonstrating the universality of our approach of using *t*BuSiOH-POM to achieve superior electron transfer towards cathode.

Experimental

Synthesis of lacunary POM materials

Details on the synthesis of α -K₉[PW₉O₃₄].16H₂O were given elsewhere.⁴⁴ To a well stirred suspension of α -K₉[PW₉O₃₄].16H₂O (10 g, 3.48 mmol) in dry MeCN (200 mL) under argon solid *n*Bu₄NBr (6 g, 18.6 mmol) were added and then *t*BuSiCl₃ (2.1 g, 10.1 mmol) and the mixture was stirred overnight at 0 °C. After separation of the white solid (KCl + KBr), white crystals of (*n*Bu₄N)₃[PW₉O₃₄(*t*BuSiOH)₃] formed upon slow evaporation of the resulting solution in an open vessel at room temperature.⁴⁷

Titanium dioxide layer preparation

FTO-coated glass (Pilkington TEC 15, <15 Ohms sq⁻¹) was cleaned by sonication in a detergent solution (Hellmanex III, Hellma Analytics), water and ethanol, followed by treatment in an oxygen plasma for 5 min. A solution of 13 μ L of concentrated aqueous HCl in 5 mL of isopropanol was slowly added to a stirred solution of titanium isopropoxide (711 mg, 2.5 mmol) in 5 mL of dry isopropanol. The cleaned substrates were spin-coated at 2000 rpm with this titania precursor solution and immediately placed on a hotplate at 150 °C. Subsequently, the samples were calcined in air at 500 °C for 45 min (1 h ramp).

Zinc oxide layer preparation

A 0.5 M ZnO sol-gel was prepared using zinc acetate dehydrate (Sigma Aldrich) in ethanolamine and 2-methoxyethanol. The mixture was stirred until completely dissolved and was subsequently filtered using a PVDF 0.45 mm filter. Fluorine doped tin oxide conducting substrates (FTO) from Solaronix (TCO10-10) were sequentially cleaned ultrasonically with soap water, distilled water, acetone and isopropanol. The substrates were introduced into an oxygen plasma chamber for 7 min prior to ZnO coating.

The ZnO films were prepared from a two-step spin coating procedure as follows: an amount of ZnO sol-gel was poured onto the substrate to fully cover it and was spin coated at 6000 rpm (acceleration 6000 rpm for 40 s). The films were immediately put on a pre-heated hot-plate at 80 °C. The substrates were annealed at 250 °C for 10 min. Once cooled down to 60 °C, the same procedure was repeated.

Device fabrication

Polymer solar cells were fabricated on 50 nm thick ZnO and TiO₂ films on FTO substrates. Then a *t*BuSiOH-POM film was deposited *via* spin coating a 5 mg mL⁻¹ solution in acetonitrile at 1000 rpm for 40 s. P3HT:IC₆₀BA blends were spin coated inside an argon filled glove box at 800 rpm for 30 s from solution consisting of 17 mg mL⁻¹ P3HT and 17 mg mL⁻¹ IC₆₀BA (P3HT was purchased from Rieke metals and IC₆₀BA was purchased from Ossila) in 1,2-dichlorobenzene and left to dry for 30 min before heating at 150 °C for 10 min. Then, an approximately 20 nm-thick under-stoichiometric molybdenum oxide (MoO_x) layer was deposited on top of the active layer to serve as the hole extraction layer.⁴⁸ The devices were completed with a 150 nm thick aluminium anode, deposited on a dedicated thermal evaporator at a pressure of 10⁻⁶ Torr through a shadow-mask, which defined the active area of the device to be equal to 12.56 mm².

Measurements and instrumentation

X-ray photoelectron spectra (XPS) and ultraviolet photoelectron spectra (UPS) were recorded using a Leybold EA-11 electron analyzer operating in constant energy mode at a pass energy of 100 eV and at a constant retard ratio of 4 eV for XPS and UPS respectively. All binding energies were referenced to the C 1s peak at 284.8 eV of surface adventitious carbon, respectively. The X-ray source for all measurements was an unmonochromatized MgK α line at 1253.6 eV (12 keV with 20 mA anode current). The valence band spectra of titanium and zinc oxide without and with *t*BuSiOH-POM were evaluated after recording the UPS spectra of metal oxide and metal oxide/POM films deposited on an FTO substrate. For the UPS measurements, the He I (21.22 eV) excitation line was used. A negative bias of 12.22 V was applied to the samples during UPS measurements in order to separate secondary electrons originating from the sample and the spectrometer and to estimate the absolute work function value from the high BE cut-off region of the UPS spectra. The analyzer resolution is determined from the width of the Au Fermi edge to be 0.16 eV. The steady-state photoluminescence spectra of P3HT on various substrates were acquired by means of a Fluoromax spectrometer (Horiba) upon excitation at 550 nm. The films were placed on a specific holder for solid samples and the spectra were corrected for the sensitivity of the detector. The PL dynamics of the samples were studied under magic angle conditions, by using a femtosecond upconversion technique. The excitation of the samples was realized by means of the second harmonics of a Ti:Sapphire laser at 410 nm. The average power was less than 3 mW while the repetition frequency was 80 MHz. The PL of the samples was collected and focused

together with the remaining fundamental fs laser beam on a 0.5 mm BBO crystal to produce frequency mixing. The upconverted beam passed through an iris, filters and a monochromator and was detected using a photomultiplier. The Instrument's Response Function (IRF) was approximately 150 fs. A bi- or three-exponential function convoluted with the IRF was used for fitting the dynamics. Absorption, transmittance and reflectance measurements were taken using a Perkin Elmer Lambda 40 UV/vis spectrophotometer. The thicknesses of films were measured using an Ambios XP-2 profilometer or a M2000 Woolam ellipsometer. The surface morphology of films was analyzed using an NT-MDT atomic force microscope (AFM) operating in tapping mode with the frequency set at 1 Hz. Current density-voltage characteristics of the fabricated solar cells were measured using a Keithley 2400 source-measure unit. Cells were illuminated using a Xe lamp and an AM 1.5G filter to simulate solar light illumination conditions with an intensity of 100 mW cm⁻² (1 Sun), as was recorded using a calibrated silicon photodiode. EQE measurements were carried out using an Autolab PGSTAT-30 potentiostat, with a 300 W Xe lamp in combination with an Oriel 1/8 monochromator for dispersing the light in an area of 0.5 cm². A Thorlabs silicon photodiode was used for the calibration of the spectra. All measurements were performed in air.

Computational methodology

Spin-polarized calculations for the isolated *t*BuSiOH-POM were performed using the Vienna Ab Initio Simulation Package (VASP). Plane-wave basis sets and the Perdew-Burke-Ernzerhof (PBE) functional were used along with the Grimme DFT-D2 method, taking into account spin-orbit coupling. Geometry optimization was carried out with maximum atomic forces set at 0.01 e Å⁻¹; initial atomic coordinates of the molecular structure were taken from work done by Zhang *et al.*⁴⁹ The Density of States (DOS) was extracted using the projector augmented wave (PAW) method, with a plane-wave cut-off energy of 400 eV and a Γ centered *k*-point grid of 2 × 2 × 2. Gaussian smearing with a width of 0.05 eV was used to determine how partial occupancies are set for each wave-function. Finally, the POM supercell was modeled within a simple cubic cell of dimensions $a = 20 \text{ \AA}$.

Results and discussion

Efficiency and stability enhancement of PSCs using *t*BuSiOH-POM

A simple, and low-cost synthetic procedure of *t*BuSiOH-POM providing high-yield is given in the Experimental section. In general, starting from the trivalent highly-charged tungstophosphate [PW₉O₃₄]⁹⁻, it has been possible to graft directly tertiary butyl (*t*Bu)-silanol moieties and an “open-structure” derivative was obtained which retains its trifold rotational symmetry. The detailed material characterization in solution, using FTIR, UV-vis, ³¹PNMR, ¹HNMR spectroscopy and cyclic voltammetry, is presented in the ESI† (Fig. S1-S3). Notably, the lowest unoccupied molecular orbital (LUMO) of the functionalized

POM was calculated at -4.38 eV (Fig. S3, ESI[†]) and is well aligned to the bottom of the conduction band (CB) of TiO_2 and ZnO ,⁵⁰ while its highest occupied molecular orbital (HOMO) is placed at -8.32 eV indicating excellent hole blocking capability of the material. The coverage of TiO_2 and ZnO with the POM film was monitored using X-ray photoelectron spectroscopy (XPS) of the $\text{TiO}_2/t\text{BuSiOH-POM}$ and $\text{ZnO}/t\text{BuSiOH-POM}$ interfaces (Fig. S4 and S5, ESI[†]) which clearly shows the $W4f$ peaks of the PW_9O_{34} parent compound and the $\text{Si } 2p$ and $\text{N } 1s$ of the functional groups confirming that the functionalized POM is present on the metal oxide surfaces. In addition, the XPS peaks reveal a significant degree of reduction (under-stoichiometry) of POMs on metal oxides, as concluded from the appearance apart from the well-defined doublet, characteristic of the W^{6+} states, of a peak at lower BEs which is attributed to lower (W^{5+}) oxidation states of the WO_3 units. The reduction of POMs has previously been considered to be the origin of improved electron transport and increased electron mobility of those materials.⁴⁴

The effect of a $t\text{BuSiOH-POM}$ film spin-coated on metal oxides from a solution in acetonitrile on the device performance was evaluated in PSCs using the device architecture of $\text{FTO}/\text{CIL}/t\text{BuSiOH-POM}/\text{P3HT}:\text{IC}_{60}\text{BA}/\text{MoO}_x/\text{Al}$ where the CIL was either TiO_2 or ZnO (Fig. 1a). In addition, PSCs without $t\text{BuSiOH-POM}$ were used as the reference devices. The chemical structures of organic semiconductors used in this study and of

$t\text{BuSiOH-POM}$ are shown in Fig. 1b, where the anchoring of the functionalized POMs on the TiO_2 or ZnO surface *via* silanol linker groups is also illustrated.⁴⁶ The transmittance spectra of TiO_2 and ZnO films on glass substrates before and after coverage with the POM film are shown in Fig. 1c. A small increase of the transmittance of metal oxide layers upon POM coating is observed, which is beneficial for the device performance since more light passes through the $\text{FTO}/\text{metal oxide}/\text{POM}$ interfaces to be absorbed from the photoactive blend. Note that the absorption spectra and bandgap of TiO_2 and ZnO films remained unaffected upon POM deposition (Fig. S6 and S7, ESI[†]).

Fig. 1d presents the current density–voltage (J - V) characteristics of the above four kinds of devices under 1 Sun (100 mW cm^{-2}) illumination using a AM 1.5G filter. The corresponding dark J - V curves are shown in Fig. 1e. Table 1 presents the overall photovoltaic performance of the devices. Compared to the reference devices, those with the $t\text{BuSiOH-POM}$ resulted in a simultaneous enhancement in the V_{oc} , J_{sc} and FF irrespective of the metal oxide interlayer. Specifically, for the TiO_2 based devices J_{sc} increased from 9.58 mA cm^{-2} to 10.66 mA cm^{-2} , V_{oc} from 0.78 V to 0.83 V and FF from 0.63 to 0.73 thus boosting the PCE from 4.71% to 6.46% ; the latter represents a 37% enhancement as compared to the reference cell. Similarly, the PCE of the ZnO based device was increased from 5.03% to 6.51% , which, to the authors' knowledge, is among the highest

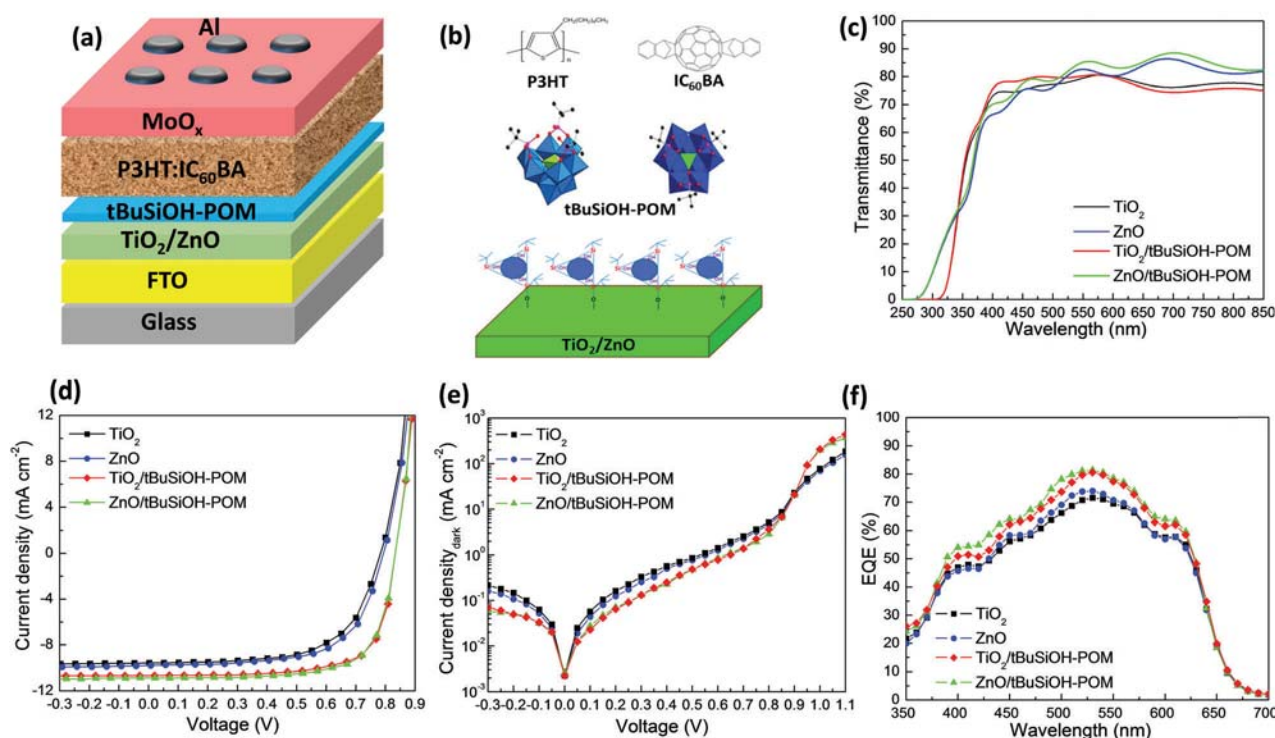


Fig. 1 (a) The inverted PSC architecture used in this study. (b) The chemical structures of the organic semiconductors used in the photoactive layer of PSC devices (up) and the polyhedral representation of $t\text{BuSiOH-POM}$ where WO_6 octahedra appear in blue color, the PO_4 tetrahedron appears in green color, and Si , C and O appear in pink, black and red color, respectively (middle). Coordination of $t\text{BuSiOH-POM}$ to the TiO_2 or ZnO substrate *via* the formation of Si-O-Ti/Zn bonds (bottom). (c) Transmittance spectra of as-deposited and $t\text{BuSiOH-POM}$ coated TiO_2 and ZnO films on glass/ FTO substrates. (d) J - V characteristics under 1.5 AM illumination of P3HT: IC_{60}BA -based devices fabricated on FTO/TiO_2 or FTO/ZnO substrates without and with $t\text{BuSiOH-POM}$. (e) The dark J - V characteristics and (f) the EQE spectra of PSCs without and with $t\text{BuSiOH-POM}$.

Table 1 Device characteristics of polymer solar cells having the device configuration FTO/TiO₂ or ZnO/*t*BuSiOH-POM/P3HT:IC₆₀BA/MoO_x/Al (mean values and standard deviations were extracted from a batch of 20 independent devices)

CIL	J_{sc} (mA cm ⁻²)	$J_{sc(EQE)}$ (mA cm ⁻²)	V_{oc} (V)	FF	PCE (%)	R_s (Ω cm ²)	R_{sh} (Ω cm ²)
TiO ₂	9.58 (±0.15)	9.68	0.78 (±0.01)	0.63 (±0.01)	4.71 (±0.13)	4.9	3821
ZnO	9.80 (±0.09)	9.81	0.79 (±0.01)	0.65 (±0.01)	5.03 (±0.11)	3.8	2557
TiO ₂ / <i>t</i> BuSiOH-POM	10.66 (±0.14)	10.62	0.83 (±0.01)	0.73 (±0.01)	6.46 (±0.09)	1.6	6586
ZnO/ <i>t</i> BuSiOH-POM	10.89 (±0.10)	10.86	0.83 (±0.01)	0.72 (±0.01)	6.51 (±0.10)	1.4	6297

efficiencies obtained in PSCs based on the P3HT:IC₆₀BA system,⁵¹ which is usually selected as the front cell active material in tandem PSCs.⁵ In this context, the devices using the ZnO CIL were always slightly over performing as compared to their counterparts based on TiO₂ probably due to the higher transparency and n-type conductivity of ZnO.⁵² The increase in the FF and the carrier collection efficiency is related to the significant decrease of the series resistance, R_s , and the large increase of the shunt resistance, R_{sh} , (Table 1) which indicate an overall enhanced quality of the cathode contact of the POM-modified devices.

Additionally, the observed increase in V_{oc} could be ascribed to the suppression of the dark reverse saturation current which is correlated with the enhanced built-in voltage of the modified devices, as evidenced by the dark J - V characteristics (Fig. 1e). In the devices with as-deposited TiO₂ or ZnO CILs, the low built-in field results in higher carrier accumulation and recombination inside the cell, thus leading to large dark reverse saturation current.^{53,54} When *t*BuSiOH-POM is embedded at the cathode interface, the built-in field is largely increased suggesting a suppression in carrier accumulation and recombination, as also evident from the decreased reverse saturation current. The enhancement in J_{sc} can be associated with a more effective photon-to-electron conversion efficiency in the POM-modified devices as shown in Fig. 1f where the corresponding external quantum efficiency (EQE) spectra of the devices before and after the insertion of POMs are presented. The EQE values of the POM-modified PSCs are significantly higher in the wavelength range of 450–650 nm (which is the absorption range of P3HT) than those of the reference devices, which is consistent with the tendency of J_{sc} of the PSCs based on different CILs. In addition, the EQE spectra of the devices were integrated from 300 to 800 nm and $J_{sc(EQE)}$ values were calculated and listed in Table 1. Notably, these values are very consistent with the J_{sc} obtained from J - V characteristics under illumination indicating the reliability of the measured J_{sc} .^{55,56}

The better performance of the devices with *t*BuSiOH-POM was also supported by the dependence of the net photocurrent density (J_{ph}) on the effective voltage (V_{eff}), where J_{ph} is equal to $J_L - J_D$ (J_L and J_D are the current density under 1.5 AM illumination and dark conditions, respectively) and V_{eff} is equal to $V_0 - V$ (V_0 is the voltage at $J_{ph} = 0$ and V is the applied voltage).^{57,58} From Fig. 2a it becomes evident that J_{ph} is larger and reaches saturation (J_{sat}) at a smaller effective voltage for both kinds of POM embedding devices as compared to the reference ones. This indicates that incorporation of *t*BuSiOH-POM into the device facilitates exciton dissociation into free carriers, and both the exciton generation rate and the dissociation

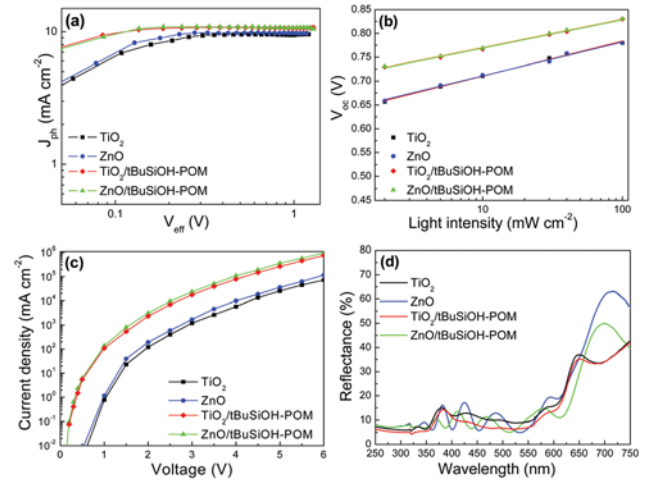


Fig. 2 Dependence of (a) net photocurrent density on effective voltage and (b) V_{oc} on 1.5 AM light intensity of P3HT:IC₆₀BA-based devices fabricated on FTO/TiO₂ or FTO/ZnO substrates without and with *t*BuSiOH-POM. (c) Current density–voltage (J - V) curves (measured in dark) in a semi-log plot of electron-only devices with the structure: FTO/TiO₂ or ZnO without and with *t*BuSiOH-POM/P3HT:IC₆₀BA/Al. (d) Reflectance spectra of the complete PSC devices.

probability were increased, thereby enhancing the photocurrent of PSCs. In particular, taking into account that the $J_{ph}/J_{ph,sat}$ ratio is related to exciton dissociation and charge collection probabilities, we found that under short-circuit conditions, the reference devices based on TiO₂ and ZnO give the $J_{ph,sc}/J_{ph,sat}$ ratios of 92.1% and 93.0%, respectively. The $J_{ph,sc}/J_{ph,sat}$ ratios of the corresponding PSCs with *t*BuSiOH-POM are 97.0% and 97.5%, respectively which clearly implies that the PSCs with POMs exhibit better exciton dissociation and enhanced charge extraction and collection. Accordingly, we infer that the best photovoltaic performance of the functionalized POM PSCs originates from enhanced exciton dissociation but also from reduced trap-assisted recombination. The reduced recombination losses of the POM-modified cells were further probed by measuring the dependence of V_{oc} on the illuminated light intensity, as shown in Fig. 2b, where the log-linear plots of V_{oc} as a function of the light intensity are presented. The slope values of V_{oc} were decreased significantly from 1.24 and $1.20k_B T/q$ to 1.02 and $1.01k_B T/q$ upon POM insertion into the TiO₂ and ZnO-based cells, respectively, where k_B is Boltzmann's constant, T is the absolute temperature, and q is the elementary charge. The relatively large slopes of the reference devices indicate an increased number of trap assisted Shockley–Read–Hall monomolecular recombination losses.^{59–61} The decreased slopes of POM embedding devices indicate a much lower trap

assisted recombination at open circuit and an enhancement of cathode selectivity. They also imply that the insertion of POMs into the vicinity of the cathode interface effectively improves the charge transport ability as also evidenced by the $J-V$ curves of electron-only devices shown in Fig. 2c. This improvement in the electron current density can be related to a decrease of the electron extraction barrier upon t BuSiOH-POM insertion. The enhanced electron current is related to the improved J_{sc} in the PSCs with the functionalized POM. The higher absorption of the POM-modified cells also contributes to the enhancement in J_{sc} . As shown in Fig. 2d, where the reflectance spectra of the complete PSCs under study are presented, the lower reflectivity of the POM-modified devices in the whole spectrum indicates stronger absorption of the incident light.

Thereafter, we monitored the stability of the four kinds of PSCs. The PSC devices for shelf time stability tests were intentionally unencapsulated, stored in the dark inside a nitrogen filled desiccator between measurements, and measured under ambient conditions (temperature 20–25 °C and a relative humidity of 25–40%). As shown in Fig. 3d, the PCEs of typical reference devices based on metal oxide CILs decreased to 90% of their initial values (T_{90}) in about three days while they diminished to 50% (T_{50}) after less than a month.

In striking contrast, the typical devices using t BuSiOH-POM coated metal oxide CILs demonstrated superior stability and maintained more than 90% of the original device PCE (T_{90}) after 1000 h. The variation of key photovoltaic performance parameters *versus* storage time is presented in Fig. 3a–c. Such exceptional temporal stability can be attributed to the functionalized POM, which forms an internal passivation layer on metal oxide CILs. It is well known that surface defects of TiO_2 and ZnO act as binding sites for the adsorption of oxygen and water molecules, which are detrimental to the ambient stability of the

devices. We speculate that the anchoring of t BuSiOH-POM on the metal oxide surface *via* the formation of strong Si–O–metal bonds, induces effective surface passivation thus preventing the formation of oxygen-induced trap states,^{62,63} while also prevents access of water to the metal oxide/photoactive layer interface. In addition, the tertiary butyl hydrophobic component of POM forms an internal stable hydrophobic encapsulating layer between the organic film and metal oxide layers retarding the degradation of both electrodes and photoactive materials, leading to more stable devices.

Surface properties of metal oxide/ t BuSiOH-POM CILs

The dependence of solar cell performance parameters on t BuSiOH-POM suggests that more details need to be known about the morphology of the deposited films so as to investigate how such factor may contribute to the improved device performance. Atomic force microscopy (AFM) was used to monitor the surface morphology of TiO_2 and ZnO before (Fig. 4a and c) and after coverage with t BuSiOH-POM (Fig. 4b and d). The TiO_2 and ZnO films (~ 50 nm) deposited on FTO present root mean square (RMS) roughness values of 3.2 and 5.7 nm, respectively. After the insertion of the POM interlayer the surface of the modified metal oxides becomes smoother with RMS roughness values of 2.5 and 4.9 nm, respectively. The physical contact between metal oxide and photoactive blend might be enhanced by a decrease in surface roughness. Another critical parameter, the surface energy, can have its own impact on the investigated system. In the case of PSCs, the surface energy can play a significant role in the formation of the morphology by directing the phase-separation process during deposition. Surface modification of metal oxides with t BuSiOH-POM can change their wettability and thus the surface energy altering the way in which the subsequently deposited organic photoactive blend assembles and orients itself on the surface. Changes in wettability were confirmed by measuring the contact angle of water and calculating surface energy (Fig. S8, S9 and Table S1, ESI[†]) of the different substrates. The as-deposited TiO_2 and ZnO substrates are rather hydrophilic showing relatively low water contact angles of 45.0° and 46.7°, respectively, and high surface energies of 58.74 and 59.47 $mJ m^{-2}$ whereas water contact angles of 52.1° and 54.2° and surface energies of 52.62 and 53.93 $mJ m^{-2}$ were measured for the POM-coated TiO_2 and ZnO substrates, respectively. It has been previously suggested that, as the hydrophilicity and surface energy of the metal oxide layer are reduced to a moderate value (around 50 $mJ m^{-2}$),⁶⁴ its interfacial contact with the photoactive blend is enhanced. The tertiary butyl (t Bu)-silanol group was selected as the hydrophobic component of the functionalized POM in order to adjust its wetting properties and achieve desirable surface energies,⁶⁵ to guarantee sufficient hydrophobicity and to enable better adhesion of the photoactive overlayer. Note that, higher hydrophobicity may also result in enhanced stability and explain/justify the observed behavior under aging in ambient air. In fact, the existence of a hydrophobic interlayer makes more difficult the adsorption of water molecules and endows the device with humidity repellent functionality. The nanomorphology of the photoactive blend

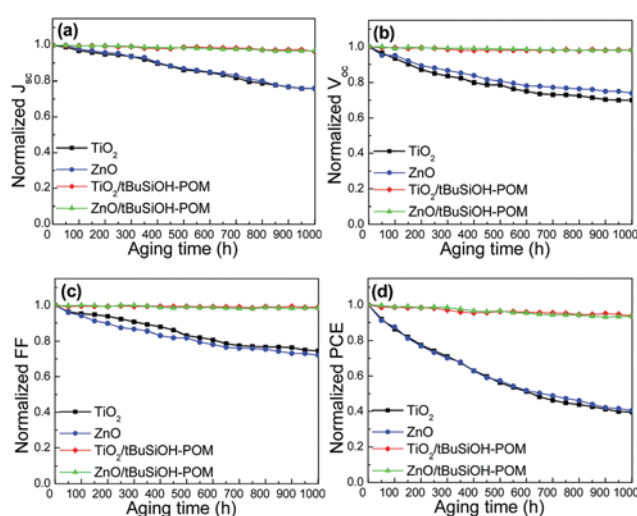


Fig. 3 Stability measurements: variation (as derived from measurements on 5 individual devices of each kind) of normalized (a) J_{sc} , (b) V_{oc} , (c) FF and (d) PCE, over a period of 1000 hours for P3HT:IC₆₀BA-based devices using TiO_2 and ZnO without and with t BuSiOH-POM.

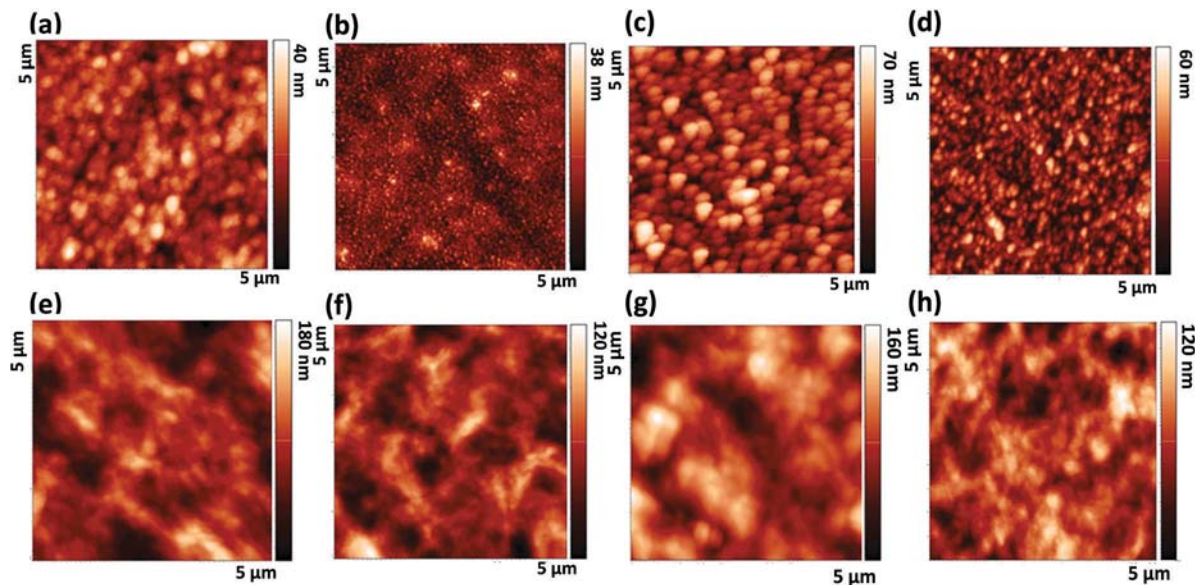


Fig. 4 2D $5 \times 5 \mu\text{m}^2$ AFM topography of (a) as-deposited TiO_2 and (b) $t\text{BuSiOH-POM}$ coated TiO_2 films, of (c) as-deposited ZnO and (d) $t\text{BuSiOH-POM}$ coated ZnO films. 2D AFM surface topography ($5 \times 5 \mu\text{m}^2$) of P3HT:IC₆₀BA films deposited on (e) TiO_2 and (f) $t\text{BuSiOH-POM}$ coated TiO_2 films, on (g) ZnO and (h) $t\text{BuSiOH-POM}$ coated ZnO films.

on TiO_2 and ZnO films without (Fig. 4e and g) and with $t\text{BuSiOH-POM}$ (Fig. 4f and h) was studied using AFM. 2D $5 \times 5 \mu\text{m}^2$ topography images of P3HT:IC₆₀BA spin-coated on as-deposited and POM-coated metal oxide substrates and reveal that the distribution of the P3HT donor and the IC₆₀BA acceptor and their interpenetrating networks are quite different. In particular, smaller donor:acceptor domains, an indication of finer, smaller scale phase separation, are formed when photoactive blends are deposited on POM-coated TiO_2 and ZnO . In addition, a significant reduction in the RMS roughness of the blend deposited on POM-modified TiO_2 (8.35 nm) and ZnO (8.22 nm) as compared to the blends deposited on as-deposited TiO_2 (16.55 nm) and ZnO (14.63 nm) is observed. The above results indicate that the film formation and physical contact at the metal oxide/ $t\text{BuSiOH-POM}$ /photoactive layer interfaces are more uniform and should lead to better electrical contact, which are beneficial to the exciton charge separation and charge transport.

$t\text{BuSiOH-POM}$ -induced changes in metal oxides W_F

The primary requirement of cathode interlayers lies in their ability to lower the W_F of the electrode by producing large interfacial dipoles that induce a downward vacuum-level shift. To test this in the case of $t\text{BuSiOH-POM}$ modified metal oxides, ultraviolet photoelectron spectroscopy (UPS) was used to probe the electronic properties of TiO_2 (Fig. 5a) and ZnO (Fig. 5b) before and after POM coverage. It is observed that, upon deposition of a thin POM layer, the cut-off region of the UPS spectra shifted towards higher binding energy, indicating a reduction in the magnitude of the W_F of TiO_2 and ZnO . In particular, the W_F of TiO_2 (4.4 eV) is shifted to 3.6 eV and that of ZnO (4.5 eV) is shifted to 3.7 eV upon POM coverage. The W_F change (ΔW_F) is 0.8 eV in both cases. Such a significant W_F

change can be probably attributed to the polar nature of the terminal $-\text{OH}$ groups of the functionalized POM. Fig. S10 (ESI[†]) shows the near Fermi level region of the $\text{TiO}_2/t\text{BuSiOH-POM}$ interface in more detail; the spectrum exhibits an extra emission peak at 1.5 eV. This peak can be attributed to photoelectrons coming from the LUMO of $t\text{BuSiOH-POM}$ which is filled upon electron transfer from trap states of TiO_2 lying just below the CB of the latter. Such electron transfer results firstly in the effective surface passivation of TiO_2 and secondly in the reduction and, therefore, the increased electron conductivity of the functionalized POM.⁴⁰ Both are beneficial for the device performance.

The decreased W_F of POM/metal oxide cathodes can also increase the built-in field used to break the electrical symmetry inside the cells which is beneficial to charge extraction efficiency. The reduction in W_F associated with the $t\text{BuSiOH-POM}$ dipole layer is illustrated in the energy diagram of the cathode interfaces presented in Fig. 5c and d. It is observed that upon POM coverage of metal oxides their W_F is significantly reduced by 0.8 eV which implies that the vacuum level shifts through the formation of a large interfacial dipole with the negative pole pointing away from the POM-modified oxide surface (Fig. 5d). This implies that the band offset for electron transfer from the IC₆₀BA LUMO to the conduction band of metal oxides decreases thus providing barrier-free electron transport under short-circuit conditions and further enhances the built in field, thus facilitating charge extraction. Note that, the low W_F values of $t\text{BuSiOH-POM}$ /metal oxide electrodes allow them to form better contacts not only with the P3HT:IC₆₀BA blend but also with the P3HT:PC₇₁BM and PTB7:PC₇₁BM ones, as can be concluded from the performance enhancement obtained in POM modified devices using those blends as the photoactive layers.

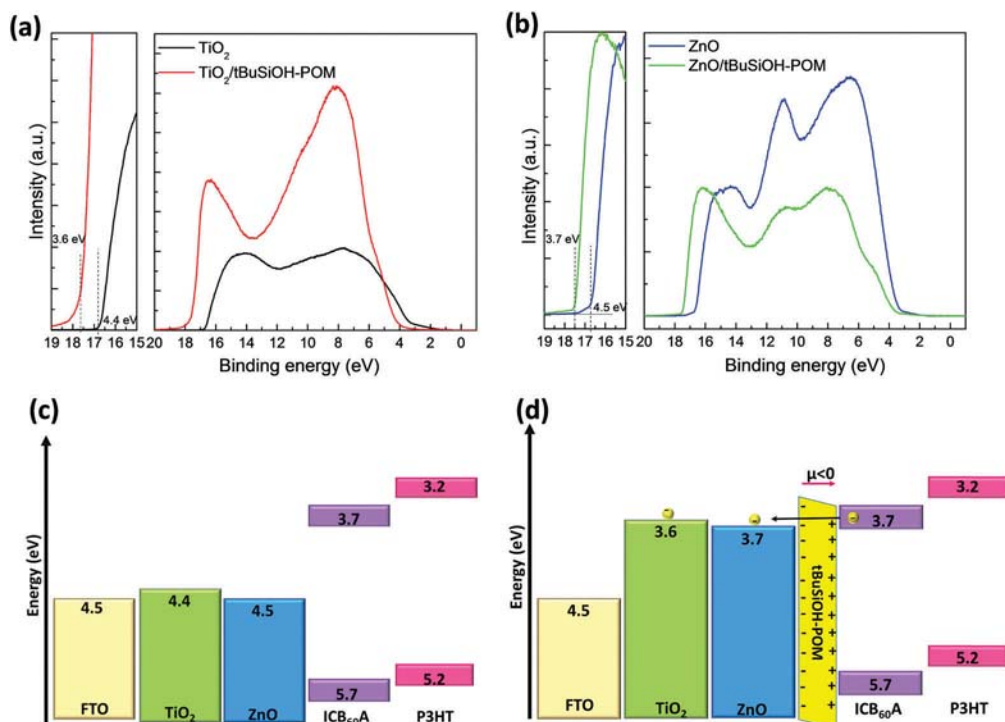


Fig. 5 UPS measurements of (a) as-deposited and *t*BuSiOH-POM coated TiO₂ and (b) as-deposited and *t*BuSiOH-POM coated ZnO films. (c) Energy level (W_F values for FTO, TiO₂ and ZnO and HOMO/LUMO levels for P3HT and ICB₆₀BA) alignment at various cathode interfaces of the inverted devices considering vacuum level alignment. (d) Illustration of the formation of a negative interfacial dipole at the metal oxide/*t*BuSiOH-POM/ICB₆₀BA interface.

In particular, the PCE of P3HT:PC₇₁BM-based devices increased from 3.17% (for the reference device using TiO₂) and 3.41% (for the reference device using ZnO) to 4.41% and 4.42%, respectively, upon POM coverage of metal oxides (Fig. S11 and Table S2, ESI[†]). Similarly, the PCE of PTB7:PC₇₁BM-based devices increased from 6.37% and 6.65% to 8.03% and 8.23%, upon POM coverage of TiO₂ and ZnO, respectively (Fig. S12 and Table S3, ESI[†]). Notably, the deposition of *t*BuSiOH-POM directly on ITO substrates remarkably enhanced the electron selective capability of the latter as demonstrated from the significant efficiency enhancement of PSCs with the structure ITO/*t*BuSiOH-POM/P3HT:ICB₆₀BA/MoO₃/Al up to 4.22% which represents a huge enhancement as compared to 0.29% of the reference cells without POM (Fig. S13 and Table S4, ESI[†]). This result shows that *t*BuSiOH-POM aside from the electron transfer mediation to TiO₂ and ZnO CILs can be also used as an efficient electron transport interlayer directly deposited on cathode electrodes; however, further investigation is needed.

Theoretical investigation of *t*BuSiOH-POM induced surface passivation of metal oxides

In order to further explore the effect of surface passivation due to electron transfer between the oxide surfaces and the POM adsorbate, as indicated previously *via* UPS measurements, the electronic structure of the latter was studied *via* density functional theory (DFT) following the procedure described in the computational methodology section. After optimizing the molecular structure of the isolated compound (Fig. S14, ESI[†]), the total density of states as well as the projected density of states

from individual atom contributions was extracted and plotted in Fig. 6. It is observed that the valence band maximum (VBM) is located at -0.1 eV below the Fermi level (0 eV) and consists of O 2p, C 2p, and H 1s orbitals with a mild hybridization from Si 3p and W 5d orbitals. It is interesting to see that the DOS also shows a sharp peak of unoccupied states in the middle of the band gap, which is contributed primarily by C 2p, O 2p and H 1s orbitals with minimal hybridization from Si 3p and W 5d orbitals. The location of this peak indicates that effective energy level alignment at the interface between the metal oxide surface and the POM may favor electron transfer from metal-oxide surface trap states to the POM adsorbate. This would provide a route for metal oxide surface passivation and instigate a downward vacuum level shift causing the reduction of the POM-modified surface work function of the metal oxides as observed experimentally.

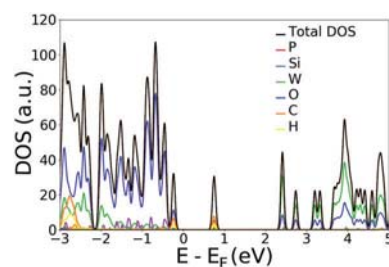


Fig. 6 Total density of states of the isolated *t*BuSiOH-POM compound as well as individual contributions from its constituent atoms. The Fermi level is located at 0 eV.

Electron transfer mediating capability of *t*BuSiOH-POM

A key motivation for this work is to see if the metal oxide/organic interface can be affected by the electron shuttling efficiency of POMs. To investigate the electron transfer mediating capability of *t*BuSiOH-POM from the photoactive layer to metal oxides we first monitored the steady-state photoluminescence (PL) of P3HT and P3HT:IC₆₀BA films on TiO₂ and ZnO before and after POM coverage. In Fig. 7a and c we show the PL spectra of the P3HT films deposited on TiO₂ and ZnO layers, respectively, with and without the POM modification. We observe the characteristic emission peaks of P3HT at around 650 and 720 nm corresponding to the 0-0 transition and the 0-1 and 0-2 sidebands.⁵⁴ The PL intensity of P3HT on metal oxides, especially on TiO₂, is significantly reduced upon POM coverage, which is an indication of the enhanced electron accepting capability of *t*BuSiOH-POM. Noteworthy is the reduction in the PL intensity of P3HT:IC₆₀BA blend films on POM-modified substrates (Fig. S15, ESI[†]), indicating that *t*BuSiOH-POM successfully mediates electron transfer from the P3HT to the TiO₂ and ZnO CB and its performance as an interfacial electron shuttle does not vanish in the presence of a strong electron acceptor such as IC₆₀BA.

Time-resolved photoluminescence (TRPL) measurements were carried out only on neat P3HT films deposited on metal oxide and metal oxide/*t*BuSiOH-POM substrates because the fullerene in the blend films causes a strong fluorescence quenching *via* the (intended) charge transfer, thus making it difficult to probe changes in the exciton lifetime in samples with and without POMs at the metal oxide/photoactive blend interfaces. We elucidated the electron transfer mediating capability of POMs by analyzing the exciton decay dynamics at the metal oxide/POM/organic interfaces. Such emission studies only probe the excited state of P3HT, so faster electron transfer

should increase the emission decay rate. Fig. 7b and d show the normalized transient PL decay curves obtained with a femtosecond laser of the P3HT/TiO₂ and P3HT/ZnO films, respectively, before and after POM interfacial modification. The excitation wavelength was set at 410 nm and the emission wavelength at 700 nm, close to the maximum of the emission band of P3HT. We fitted the curves and obtained the corresponding decay lifetimes with a bi-exponential decay function except for the ZnO/*t*BuSiOH-POM/P3HT sample where a three-exponential function was applied (Table S3, ESI[†]). In the case of the TiO₂ substrate, the presence of *t*BuSiOH-POM dramatically accelerates the PL decay process with the average decay lifetime τ decreasing from 7.4 to 1.2 ps. This is consistent with the POM being an excellent electron acceptor/mediator to TiO₂.

However, although the POM coverage of TiO₂ granted a substantial quenching of the decay lifetime τ thus verifying the role of functionalized POM as the electron acceptor and the electron transfer mediator, it induced smaller deviation in the already higher exciton lifetime of P3HT on ZnO (from 10.3 to 9.0 ps) as compared to TiO₂. There are several factors responsible for the observed difference in the steady state and transient PL spectra of P3HT on TiO₂ and ZnO. One is the slower electron injection into ZnO than TiO₂ due to the smaller effective electron mass and, consequently, the lower density of acceptor states in ZnO.^{66,67} If the electron injection rate into ZnO is slow enough to permit competition of internal deactivation of the excited P3HT, then the electron transfer yield from the POM into ZnO decreases. A second factor is that bound charge-transfer pairs are formed, between electrons injected into the oxide CB and the positively charged P3HT species,⁶⁶ which suffer from fast recombination before full charge separation occurs, and thus the number of injected electrons in the oxide CB band decreases. This is more efficient in ZnO due to its lower dielectric constant as compared to TiO₂. POM modification restricts but not completely eliminates the formation of charge-transfer species. In addition, upon POM coating effective surface passivation of surface defect states, which are of higher density in ZnO as compared to TiO₂,⁶⁸ is expected to increase the effective exciton lifetime,^{19,69} thus acting antagonistically with the reduction in exciton lifetime caused by effective electron transfer from the LUMO of P3HT to the metal oxide CB *via* the POM path.

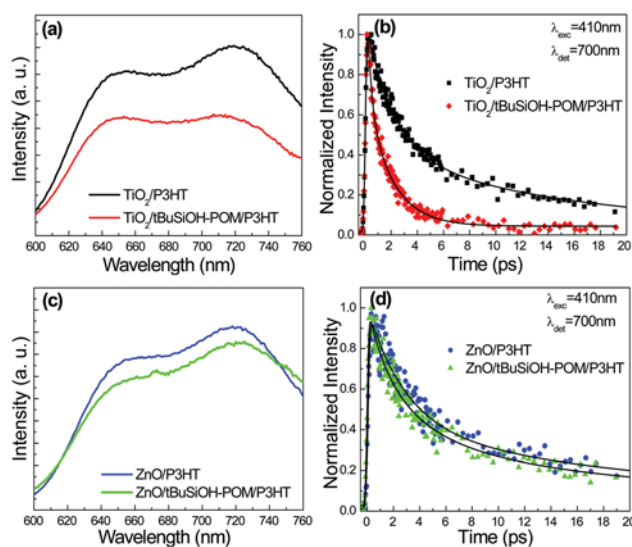


Fig. 7 (a) Steady-state and (b) transient PL dynamics of P3HT thin films on as-deposited and *t*BuSiOH-POM coated TiO₂ substrates. (c) Steady-state and (d) transient PL dynamics of P3HT thin films on as-deposited and *t*BuSiOH-POM coated ZnO substrates.

Conclusions

In conclusion, high-efficiency inverted P3HT:IC₆₀BA-based polymer solar cells with an average PCE of 6.51% were fabricated with the insertion of a silanol-functionalized polyoxometalate layer in the electron collecting contact within the inverted device structure. The efficiency enhancement of the devices mainly originates from the large reduction in the W_F of TiO₂ and ZnO cathode interlayers and from the excellent electron transfer capability of *t*BuSiOH-POM to metal oxides. In addition, the passivation of metal oxide surfaces and the corresponding decrease in the surface energy of metal oxide substrates *via*

the anchoring of silanol groups which induced better nano-morphology of the photoactive blend also contributed to improved device performance. The modified devices exhibited significantly improved lifetime retaining 90% of their initial PCEs after 1000 hours. This work obviates the laborious synthesis of appropriately functionalized polyoxometalates as effective interlayers in high efficiency and air-stable solution-processed polymer solar cells and related devices.

Conflicts of interest

There are no conflicts to declare.

Acknowledgements

A. S. acknowledges an IKY-fellowship co-financed by the European Social Fund-ESF and Greek national funds under the “Strengthening Post-Doctoral Research (MIS: 5001552)” through the Operational Program “National Human Resources Development Program, Education and Lifelong Learning” (priority axes 6, 8, 9). Y. T. and M. K. acknowledge that part of this work also has been supported by TUBITAK 2211-C program and Selcuk University BAP office (PN: 14201047). A. F. acknowledges postdoctoral funding from Alexander von Humboldt Foundation. T. P. acknowledges the use of HPC computational facilities provided by the Faculty of Science and Engineering, University of Chester, UK.

Notes and references

- 1 G. Yu, J. Hummelen, F. Wudl and A. J. Heeger, *Science*, 1995, **270**, 1789–1791.
- 2 Z. He, C. Zhong, S. Su, M. Xu, H. Wu and Y. Cao, *Nat. Photonics*, 2012, **6**, 591–595.
- 3 J. J. M. Halls, C. A. Walsh, N. C. Greenham, E. A. Marseglia, R. H. Friend, S. C. Moratti and A. B. Holmes, *Nature*, 1995, **376**, 498–500.
- 4 L. Dou, J. You, J. Yang, C.-C. Chen, Y. He, S. Murase, T. Moriarty, K. Emery, G. Li and Y. Yang, *Nat. Photonics*, 2012, **6**, 180–185.
- 5 J. You, L. Dou, K. Yoshimura, T. Kato, K. Ohya, T. Moriarty, K. Emery, C.-C. Chen, J. Gao, G. Li and Y. Yang, *Nat. Commun.*, 2013, **4**, 1446.
- 6 Y. J. Cheng, S. H. Yang and C. S. Hsu, *Chem. Rev.*, 2009, **109**, 5868–5923.
- 7 Y. Y. Liang and L. P. Yu, *Acc. Chem. Res.*, 2010, **43**, 1227–1236.
- 8 Y. F. Li, *Acc. Chem. Res.*, 2012, **45**, 723–733.
- 9 J. Peet, J. Y. Kim, N. E. Coates, W. L. Ma, D. Moses, A. J. Heeger and G. C. Bazan, *Nat. Mater.*, 2007, **6**, 497–500.
- 10 G. Li, V. Shrotriya, J. Huang, Y. Yao, T. Moriarty, K. Emery and Y. Yang, *Nat. Mater.*, 2005, **4**, 864–868.
- 11 P. M. Beaujuge and J. M. J. Frechet, *J. Am. Chem. Soc.*, 2011, **133**, 20009–20029.
- 12 J. K. Lee, W. L. Ma, C. J. Brabec, J. Yuen, J. S. Moon, J. Y. Kim, K. Lee, G. C. Bazan and A. J. Heeger, *J. Am. Chem. Soc.*, 2008, **130**, 3619–3623.
- 13 M. Vasilopoulou, A. M. Douvas, D. G. Georgiadou, V. Constantoudis, D. Davazoglou, S. Kennou, L. C. Palilis, D. Daphnomili, A. G. Coutsolelos and P. Argitis, *Nano Res.*, 2014, **7**, 679–693.
- 14 Y. M. Sun, J. H. Seo, C. J. Takacs, J. Seifert and A. J. Heeger, *Adv. Mater.*, 2011, **23**, 1679–1683.
- 15 S.-H. Liao, H.-J. Jhuo, Y.-S. Cheng and S.-A. Chen, *Adv. Mater.*, 2013, **25**, 4766–4771.
- 16 S. Chen, X. Du, G. Ye, J. Cao, H. Sun, Z. Xiao and L. Ding, *J. Mater. Chem. A*, 2013, **1**, 11170–11176.
- 17 S. Trost, K. Zilberberg, A. Behrendt, A. Polywka, P. Görrn, P. Reckers, J. Maibach, T. Mayer and T. Riedl, *Adv. Energy Mater.*, 2013, **3**, 1437–1444.
- 18 M. Prosa, M. Tessarolo, M. Bolognesi, O. Margeat, D. Gedefaw, M. Gaceur, C. Videlat Ackermann, M. R. Andersson, M. Muccini, M. Seri and J. Ackermann, *ACS Appl. Mater. Interfaces*, 2016, **8**, 1635–1643.
- 19 M. Vasilopoulou, D. G. Georgiadou, A. Soultati, N. Boukos, S. Gardelis, L. C. Palilis, M. Fakis, G. Skoulatakis, S. Kennou, M. Botzakaki, S. Georga, C. A. Krontiras, F. Auras, D. Fattakhova-Rohlfing, T. Bein, T. A. Papadopoulos, D. Davazoglou and P. Argitis, *Adv. Energy Mater.*, 2014, **4**, 1400214.
- 20 A. C. Papageorgiou, N. S. Beglitis, C. L. Pang, G. Teobaldi, G. Cabailh, Q. Chen, A. J. Fisher, W. A. Hofer and G. Thornton, *Proc. Natl. Acad. Sci. U. S. A.*, 2010, **107**, 2391–2396.
- 21 I. Lange, S. Reiter, M. Pätzl, A. Zykov, A. Nefedov, J. Hildebrandt, S. Hecht, S. Kowarik, C. Wöll, G. Heimel and D. Neher, *Adv. Funct. Mater.*, 2014, **24**, 7014–7024.
- 22 S. Bai, Y. Jin, X. Liang, Z. Ye, Z. Wu, B. Sun, Z. Ma, Z. Tang, J. Wang, U. Würfel, F. Gao and F. Zhang, *Adv. Energy Mater.*, 2015, **5**, 1401606.
- 23 S. B. Jo, J. H. Lee, M. Sim, M. Kim, J. H. Park, Y. S. Choi, Y. Kim, S.-G. Ihn and K. Cho, *Adv. Energy Mater.*, 2011, **1**, 690–698.
- 24 Z. Li, X. Zhang, C. Liu, Z. Zhang, J. Li, L. Shen, W. Guo and S. Ruan, *ACS Appl. Mater. Interfaces*, 2016, **8**, 8224–8231.
- 25 C. Sun, X. Li, G. Wang, P. Li, W. Zhang, T. Jiu, N. Jiang and J. Fang, *RSC Adv.*, 2014, **4**, 19529–19532.
- 26 D. Yang, P. Fu, F. Zhang, N. Wang, J. Zhang and C. Li, *J. Mater. Chem. A*, 2014, **2**, 17281–17285.
- 27 S. W. Heo, T. H. Huong Le, T. Tanaka, I. Osaka, K. Takimiya and K. Tajima, *J. Mater. Chem. A*, 2017, **5**, 10347–10354.
- 28 X. Lin, Y. Yang, L. Nian, H. Su, J. Ou, Z. Yuan, F. Xie, W. Hong, D. Yu, M. Zhang, Y. Mab and X. Chen, *Nano Energy*, 2016, **26**, 216–223.
- 29 S. Nam, J. Seo, S. Woo, W. H. Kim, D. D. C. Bradley and Y. Kim, *Nat. Commun.*, 2015, **6**, 8929.
- 30 M. Thambidurai, J. Y. Kim, Y. Ko, H.-J. Song, H. Shin, J. Song, Y. Lee, N. Muthukumarasamy, D. Velauthapillaic and C. Lee, *Nanoscale*, 2014, **6**, 8585–8589.
- 31 S. Trost, T. Becker, A. Polywka, P. Görrn, M. F. Oszajca, N. A. Luechinger, D. Rogalla, M. Weidner, P. Reckers, T. Mayer and T. Riedl, *Adv. Energy Mater.*, 2016, **6**, 1600347.

- 32 G. Kim, J. Kong, J. Kim, H. Kang, H. Back, H. Kim and K. Lee, *Adv. Energy Mater.*, 2015, **5**, 1401298.
- 33 T. Stubhan, I. Litzov, N. Li, M. Salinas, M. Steidl, G. Sauer, K. Forberich, G. J. Matt, M. Halik and C. J. Brabec, *J. Mater. Chem. A*, 2013, **1**, 6004–6009.
- 34 S. Trost, T. Becker, K. Zilberberg, A. Behrendt, A. Polywka, R. Heiderhoff, P. Görrn and T. Riedl, *Sci. Rep.*, 2015, **5**, 7765.
- 35 E. Polydorou, A. Zeniou, D. Tsikritzis, A. Soultati, I. Sakellis, S. Gardelis, T. A. Papadopoulos, J. Briscoe, L. C. Palilis, S. Kennou, E. Gogolides, P. Argitis, D. Davazoglou and M. Vasilopoulou, *J. Mater. Chem. A*, 2016, **30**, 11844–11858.
- 36 E. Polydorou, I. Sakellis, A. Soultati, A. Kaltzoglou, T. A. Papadopoulos, J. Briscoe, D. Tsikritzis, M. Fakis, L. C. Palilis, S. Kennou, P. Argitis, P. Falaras, D. Davazoglou and M. Vasilopoulou, *Nano Energy*, 2017, **34**, 500–514.
- 37 J. M. Sumliner, H. Lv, J. Fielden, Y. V. Geletii and C. L. Hill, *Eur. J. Inorg. Chem.*, 2014, 635–644.
- 38 M. Vasilopoulou, I. Raptis, P. Argitis, I. Aspiotis and D. Davazoglou, *Microelectron. Eng.*, 2006, **83**, 1414–1417.
- 39 M. Vasilopoulou, E. Polydorou, A. M. Douvas, L. C. Palilis, S. Kennou and P. Argitis, *Energy Environ. Sci.*, 2015, **8**, 2448–2463.
- 40 L. C. Palilis, M. Vasilopoulou, A. M. Douvas, D. G. Georgiadou, S. Kennou, N. A. Sthathopoulos, V. Constantoudis and P. Argitis, *Sol. Energy Mater. Sol. Cells*, 2013, **114**, 205–213.
- 41 M. Vasilopoulou, A. M. Douvas, L. C. Palilis, S. Kennou and P. Argitis, *J. Am. Chem. Soc.*, 2015, **137**, 6844–6856.
- 42 Y. C. Chen, S. Wang, L. W. Xue, Z. G. Zhang, H. L. Li, L. X. Wu, Y. Wang, F. H. Li, F. L. Zhang and Y. F. Li, *J. Mater. Chem. A*, 2016, **4**, 19189–19196.
- 43 Y. Chen, S. Zhang, Q. Peng, L. Wu, F. Li and Y. Wang, *J. Mater. Chem. A*, 2017, **5**, 15294–15301.
- 44 M. Tountas, Y. Topal, E. Polydorou, A. Soultati, A. Verykios, A. Kaltzoglou, T. A. Papadopoulos, F. Auras, K. Seintis, M. Fakis, L. C. Palilis, D. Tsikritzis, S. Kennou, M. Koutsourelis, G. Papaioannou, M. Ersöz, M. Kus, P. Falaras, D. Davazoglou, P. Argitis and M. Vasilopoulou, *ACS Appl. Mater. Interfaces*, 2017, **9**, 22773–22787.
- 45 E. Galoppini, *Coord. Chem. Rev.*, 2004, **248**, 1283–1297.
- 46 A. M. Love, C. A. Carrero, A. Chiericato, J. T. Grant, S. Conrad, R. Verel and I. Hermans, *Chem. Mater.*, 2016, **28**, 5495–5504.
- 47 A. Mazeaud, N. Ammani, F. Robert and R. Thovenot, *Angew. Chem., Int. Ed. Engl.*, 1996, **35**, 1961–1964.
- 48 N. Vourdas, G. Papadimitropoulos, I. Kostis, M. Vasilopoulou and D. Davazoglou, *Thin Solid Films*, 2012, **520**, 3614–3619.
- 49 D. Zhang, K. Wang, Q. Yan, P. Ma and J. Wang, *Chin. J. Inorg. Chem.*, 2012, **10**, 2236–2240.
- 50 A. Walsh and K. T. Butler, *Acc. Chem. Res.*, 2014, **47**, 364–372.
- 51 G. Zhao, Y. He and Y. Li, *Adv. Mater.*, 2010, **22**, 4355–4358.
- 52 K. D. Kim, D. C. Lim, J. Hu, J. D. Kwon, M. G. Jeong, H. O. Seo, J. Y. Lee, K. Y. Jang, J. H. Lim, K. H. Lee, Y. Jeong, Y. D. Kim and S. Cho, *ACS Appl. Mater. Interfaces*, 2013, **5**, 8718–8723.
- 53 S. A. Hawks, F. Deledalle, J. Yao, D. G. Rebois, G. Li, J. Nelson, Y. Yang, T. Kirchartz and J. R. Durrant, *Adv. Energy Mater.*, 2013, **3**, 1201–1209.
- 54 M. A. Ruderer, S. Guo, R. Meier, H.-Y. Chiang, V. Körtstgens, J. Wiedersich, J. Perlich, S. V. Roth and P. Müller-Buschbaum, *Adv. Funct. Mater.*, 2011, **21**, 3382–3391.
- 55 M. Sunderberg, O. Inganäs, S. Stafström, G. Gustafsson and B. Sjögren, *Solid State Commun.*, 1989, **71**, 435–439.
- 56 E. Zimmermann, P. Ehrenreich, T. Pfadler, J. A. Dorman, J. Weickert and L. Schmidt-Mende, *Nat. Photonics*, 2014, **8**, 669–672.
- 57 S. R. Cowan, R. A. Street, S. Cho and A. J. Heeger, *Phys. Rev. B: Condens. Matter Mater. Phys.*, 2011, **83**, 035205.
- 58 Q. Zhang, B. Kan, F. Liu, G. K. Long, X. J. Wan, X. Q. Chen, Y. Zuo, W. Ni, H. J. Zhang, M. M. Li, Z. C. Hu, F. Huang, Y. Cao, Z. Q. Liang, M. T. Zhang, T. P. Russell and Y. S. Chen, *Nat. Photonics*, 2015, **9**, 35–41.
- 59 L. Reinhardt, M. Grein, C. Bühler, M. Schubert and U. Würfel, *Adv. Energy Mater.*, 2014, **5**, 1400081.
- 60 U. Würfel, D. Neher, A. Spies and S. Albrecht, *Nat. Commun.*, 2015, **6**, 6951.
- 61 M. C. Scharber, *Adv. Mater.*, 2016, **28**, 1994–2001.
- 62 E. Ngo, S. Venkatesan, D. Khatiwada, C. Zhang and Q. Qiao, *ACS Appl. Mater. Interfaces*, 2015, **7**, 16093–16100.
- 63 J. Zhu, M. Vasilopoulou, D. Davazoglou, S. Kennou, A. Chroneos and U. Schwingenschlögl, *Sci. Rep.*, 2017, **7**, 40882.
- 64 X. Bulliard, S.-G. Ihn, S. Yun, Y. Kim, D. Choi, J.-Y. Choi, M. Kim, M. Sim, J.-H. Park, W. Choi and K. Cho, *Adv. Funct. Mater.*, 2010, **20**, 4381–4387.
- 65 S. B. Ambade, R. B. Ambade, S. S. Bagde and S.-H. Lee, *ACS Appl. Mater. Interfaces*, 2016, **8**, 35270–35280.
- 66 C. Martín, M. Ziölek, M. Marchena and A. Douhal, *J. Phys. Chem. C*, 2011, **115**, 23183–23191.
- 67 J. Sobus, G. Burdzinski, J. Karolczak, J. Idigoras, J. A. Anta and M. Ziölek, *Langmuir*, 2014, **30**, 2505–2512.
- 68 A. M. Ali, E. A. C. Emanuelsson and D. A. Patterson, *Appl. Catal., B*, 2010, **97**, 168–181.
- 69 W. Li, W. Zhang, S. Van Reenen, R. J. Sutton, J. Fan, A. A. Haghighirad, M. B. Johnston, L. Wang and H. J. Snaith, *Energy Environ. Sci.*, 2016, **9**, 490–498.